Iron Pyrite Thin Film Counter Electrodes for Dye-Sensitized Solar Cells: High Efficiency for Iodine and Cobalt Redox Electrolyte Cells

Sudhanshu Shukla,[†,‡] Nguyen Huu Loc,[§] Pablo P. Boix,[§] Teck Ming Koh,[§] Rajiv Ramanujam Prabhakar,[‡] Hemant K. Mulmudi,[§] Jun Zhang,[∥] Shi Chen,[∥] Chin Fan Ng,[∥] Cheng Hon Alfred Huan,[∥] Nripan Mathews,[‡] Thirumany Sritharan,[‡] and Qihua Xiong*[,∥,⊥]

[†]Energy Research Institute, Interdisciplinary Graduate School, [‡]School of Materials Science and Engineering, [§]Energy Research Institute, [∥]Division of Physics and Applied Physics, School of Physical and Mathematical Sciences, and [⊥]NOVITAS, Nanoelectronics Centre of Excellence, School of Electrical and Electronic Engineering, Nanyang Technological University, Singapore 639798

ABSTRACT Iron pyrite has been the material of interest in the solar community due to its optical properties and abundance. However, the progress is marred due to the lack of control on the surface and intrinsic chemistry of pyrite. In this report, we show iron pyrite as an efficient counter electrode (CE) material alternative to the conventional Pt and poly(3,4-ethylenedioxythiophene (PEDOT) CEs in dye-sensitized solar cells (DSSCs). Pyrite film CEs prepared by spray pyrolysis are utilized in I_3^-/I^- and Co(III)/Co(II) electrolyte-mediated DSSCs. From cyclic voltammetry and impedance spectroscopy studies, the catalytic activity is found to be comparable with that of Pt and PEDOT in I_3^-/I^- and Co(III)/Co(II) electrolyte, respectively. With the I_3^-/I^- electrolyte, photoconversion efficiency is found to be 8.0% for the pyrite CE and 7.5% for Pt, whereas with Co(III)/Co(II) redox DSSCs, efficiency is found to be the same for both pyrite and PEDOT (6.3%). The excellent performance of the pyrite CE in both the systems makes it a distinctive choice among the various CE materials studied.

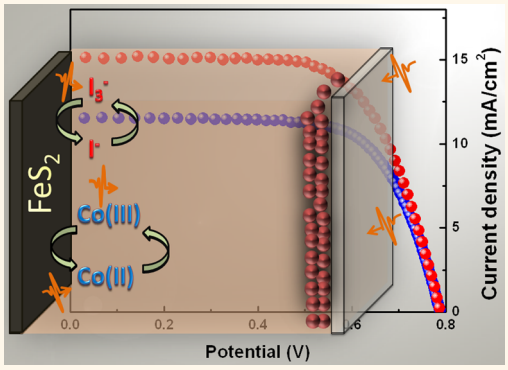

KEYWORDS: iron pyrite · dye-sensitized solar cells · counter electrode · spray pyrolysis

Iron pyrite (FeS_2) has been of continuous interest since the 1970s due to its abundance and attractive band gap. However, except for some early studies by Tributsch,[1] progress in utilizing FeS_2 as a light absorber has been slow and hampered by difficulties in stoichiometry control as well as the presence of surface accumulation layers.[2,3] Recently, nanoparticle synthesis of pyrite[4] as well as the exploration of its optoelectronic properties has received renewed interest due to its different roles in energy harvesting systems such as in sensitized solar cells,[5] as a catalyst for oxygen reduction[6] and hydrogen evolution,[7] and also as a possible hole transporter.[8] In this report, we demonstrate that pyrite thin films can function as an efficient counter electrode in dye-sensitized solar cells (DSSCs), functioning superior to the conventionally used platinum (Pt) and comparable to poly(3,4-ethylenedioxythiophene) (PEDOT) counter electrodes in (iodine/iodide) I_3^-/I^- and cobalt-based (Co(III)/Co(II)) redox electrolytes.

DSSCs hold great promise as a viable alternative to silicon-based cells,[9] especially for indoor applications. Research effort has been dedicated to reduce the cost and to the scale up of technology to commercial levels.[10,11] DSSCs comprise three major components, namely, photoanodes, photocathodes, and electrolytes.[12] At the photoanode, electrons in dye molecules excited by the photons are transferred to a wide band gap semiconductor such as TiO_2 and ZnO.[13,14] The redox couple in the electrolyte reduces the dye back to its ground state and in turn accepts the electron from the counter electrode catalyst which is usually platinum.[15,16] The I_3^-/I^--based electrolyte is commonly used in DSSCs. Because the photovoltage in the

* Address correspondence to qihua@ntu.edu.sg.

Received for review July 23, 2014 and accepted September 20, 2014.

Published online September 21, 2014
10.1021/nn5040982

DSSC depends on the redox potential of the electrolyte, the choice of electrolyte is vital. The highest efficiency DSSCs employ cobalt-based electrolytes[17,18] due to the higher difference in the Fermi level of the semiconductor (usually TiO_2) and the redox potential of the cobalt-based electrolyte. Pt or carbon is commonly used for counter electrodes in DSSCs due to their good catalytic activity.[19] Pt gives good performance, but it raises cost concerns for the cell. Carbon, on the other hand, is cheaper but exhibits lower performance.[20] Therefore, researchers have strived to develop alternative counter electrode materials which could possess the advantages of both Pt and carbon. Candidate alternative materials include transition metal oxides,[14,21,22] sulfides,[23] nitrides,[24,25] carbides,[26] and also carbon[27,28] and graphene.[29−31] Notably, the choice of counter electrode material is different for different electrolytes. Pt performs the best for I_3^-/I^- redox couples, while PEDOT is the catalyst of choice for cobalt-based electrolytes.[32−34] Herein, we report iron pyrite thin film counter electrodes with I_3^-/I^- as well as cobalt redox electrolyte DSSCs. Pyrite nanocrystals have been reported as a counter electrode with the I_3^-/I^- system.[35] It should be highlighted that the latter is more interesting as very few materials perform well with that electrolyte. However, the synthesis required to prepare pyrite films involves use of toxic solvents such as oleylamine and ethylenediamine. Also, the capping ligands limit the conductivity of the films, which is important for counter electrodes.[36]

Spray technique offers the advantage of fast processing and is an established non-vacuum-based technology which has been successfully employed for the deposition of other PV materials such as copper indium sulfide (CIS), copper indium gallium sulfide (CIGS), and copper zinc tin sulfide (CZTS).[37,38] Using water as a solvent makes it more adaptable to cheap precursors and substrates as well as compatible with existing automated or manual spraying systems. Hence this technique is adopted to produce iron pyrite thin films in this study to explore its applicability as counter electrodes in DSSCs. We have further examined the phase and structure of the films by X-ray diffraction (XRD), Raman spectroscopy, and X-ray photoelectron spectroscopy (XPS). Their morphology, characterized by scanning electron microscopy (SEM) and atomic force microscopy (AFM), was found to be rough, which is advantageous for catalytic activity. Electrical characterization of the films revealed them to be p-type with room temperature resistivity of 0.5 Ω·cm and mobility of 2.12 $cm^2(V\cdot s)^{-1}$. Low resistivity FeS_2 films prepared by spray pyrolysis were found to be comparable to Pt in catalytic activity with iodine-based electrolytes. Similarly in a cobalt-based electrolyte, the sprayed FeS_2 films showed comparable activity to that of PEDOT. Electrochemical impedance spectroscopy was performed to analyze the performance and electrochemical behavior with the electrolytes. The high performance of the pyrite solar cells here is attributed to the excellent electrochemical activity as well as the increased optical paths within the solar cells.

RESULTS AND DISCUSSION

FeS_2 thin films were prepared on a glass substrate by simple spray pyrolysis of iron and sulfur ($FeCl_3\cdot 6H_2O$ and $(NH_2)_2CS$) precursors. The concentration of the sulfur precursor was kept higher deliberately to compensate for sulfur loss during the reaction. Pyrolytic decomposition of the chemical precursors occurs at the hot surface where they form a brownish red film. However, no XRD signal could be detected from the as-sprayed films, indicating that they are amorphous (Figure S1, Supporting Information). Subsequent annealing was conducted in a sulfur environment at 400 °C for 30 min to crystallize the films and to achieve the appropriate stoichiometry. Films turned black with a shiny luster after this annealing treatment. Film thicknesses were typically 200 ± 50 nm. Figure 1 shows the XRD, Raman, and XPS data obtained in these films. All XRD peaks in Figure 1a could be indexed to the cubic FeS_2 pyrite structure. The lattice parameters are $a = 5.419$ Å, which is close to the reported value for pyrite (5.417 Å).[39] Raman spectroscopy was conducted to confirm the phase purity of the films. Figure 1b shows three peaks in Raman scan at wavenumbers of 339, 375, and 425 cm^{-1}. These correspond to A_g and E_g modes due to sulfur dumbbell stretching and the $T_g(3)$ vibrational mode, respectively, of the pyrite phase.[2,40] The other two phonon modes $T_g(1)$ at ≈350 cm^{-1} and $T_g(2)$ at ≈377 cm^{-1} were not observed due to low scattering and strong extinction at room temperature.[41] Note that marcasite, which is a common polymorph of FeS_2, whose peak positions are marked in green color for reference, is absent. Hence, it can be concluded that only the cubic pyrite phase was formed after the sulfurization treatment.

X-ray photoelectron spectroscopy was performed to evaluate the composition of the film. Figure 1c,d shows the Fe 2p and S 2p spectra, respectively. Figure 1c shows two predominant peaks at 707.5 and 720.0 eV corresponding to Fe $2p_{3/2}$ and Fe $2p_{1/2}$ doublet splitting due to spin−orbit coupling. These binding energies (BEs) are consistent with the BEs of Fe in the Fe(II)−S bond.[42] The high-energy shoulder at 709.1 eV may be attributed to defects or some Fe(III)−S bonds at the surface.[43] No oxides of Fe whose BEs are reported to be 708.4 eV (FeO) and 709.8 eV (Fe_2O_3) were detected.[44] The major peak at 162.9 eV in Figure 1d could be attributed to persulfide S_2^{2-} in FeS_2,[45] while the small peak at 162.0 eV obtained by deconvolution could be due to disulfide ions at the surface.[46,47] The minor peak at 164.5 eV was due to molecular polysulfides (S_n^{2-}). The typical morphology of the film surface is shown in the SEM scan (Supporting Information Figure S1). In spray pyrolysis, new grains are nucleated by successive spray droplets, and the films are characterized by small

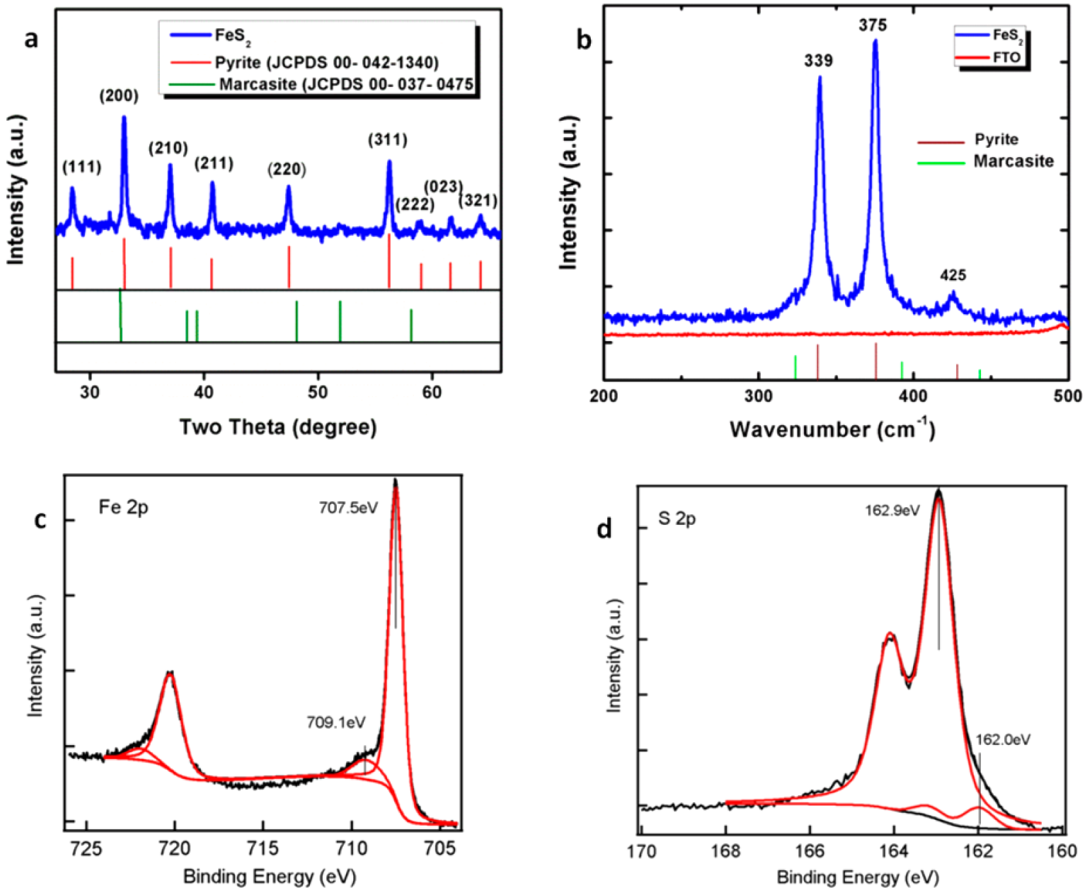

Figure 1. (a) XRD, (b) Raman spectra of the pyrite films prepared by spray pyrolysis, (c) Fe 2p and (d) S 2p XPS scans of the pyrite films.

grain size.[48] Subsequent sulfurization helps in grain growth to achieve crystalline pyrite films[49] (see Supporting Information and Figure 1).

In order for a material to behave as a good counter electrode, it has to display certain characteristics such as high conductivity (to reduce parasitic series resistance), high catalytic activity, as well as an increased number of catalytic sites. Hall measurements of the films showed high conductivity p-type behavior. The electrical properties obtained by Hall analysis are listed in Table 1 (raw data are available in Supporting Information Table ST1). The films showed good electrical conductivity, which is an important requirement for a good counter electrode. Charge carrier concentration was found to be $\sim 10^{18}$ cm^{-3}. The mobility value, calculated to be 2.12 $cm^2(V \cdot s)^{-1}$, is similar to values previously reported for pyrite films.[2] It is to be noted that, in the literature, reports concerning pyrite single crystals have generally showed n-type behavior where films have been found to be p-type, the reason for which is still a debatable issue.[3,49] The carrier density and mobility values obtained in the work may be of great interest for pyrite-based solar cells along with the p-type conductivity.

To examine the catalytic activity of pyrite cathodes, cyclic voltammetry (CV) was carried out in a three-electrode system (working electrode, reference electrode, and counter electrode). The electrolyte used was 10 mM LiI, 1 mM I_2, and 0.1 M $LiClO_4$ in acetonitrile solution. The scan rate was fixed to 100 mV s^{-1}. Positive current peaks correspond to the oxidation reaction, and negative current peaks are the reduction reaction of I_3^-/I^-. Two pairs of oxidation and reduction peaks appear in the CV scan, as shown in Figure 2 for both Pt and pyrite. Cathodic peaks signify the reduction potential at which the following reactions occur[15]

TABLE 1. Electrical Parameters of Pyrite Film Measured by Hall Analysis

parameters	numerical value
carrier density (cm^{-3})	4.90×10^{18}
resistivity ($\Omega \cdot cm$)	0.59
mobility ($cm^2/V \cdot s$)	2.12
carrier type	holes

$$I_3^- + 2e^- \rightarrow 3I^- \quad \text{at } -0.15V$$

$$3I_2 + 2e^- \rightarrow 2I_3^- \quad \text{at } 0.42V$$

These reduction potentials lie within the reported values of the reduction potentials for the above reactions.[50] The CV plot for the pyrite counter electrode closely resembles that of Pt in Figure 2, indicating that it has a similar potential to catalyze the above redox reactions. Also, reduction peaks associated with

I_2 to I_3^- and I_3^- to I^- reduction processes due to pyrite were slightly shifted to the right by approximately 0.05 V with respect to Pt peaks, signifying that the reaction occurs slightly easier for pyrite CE. Similar CV measurements were performed for the Co(III)/Co(II) redox electrolytes. Current densities obtained from CV plots showed higher values for pyrite with the Co(III)/Co(II) electrolyte in comparison to PEDOT as the counter electrode (Figure S2, Supporting Information), indicating that pyrites can be an efficient counter electrode catalyst.

Surface scans of the film done by AFM tapping mode are shown in Figure 3a–c, and the surface roughnesses of the pyrite films are found to be around 34.9 nm, and for Pt and PEDOT, the surface roughnesses are around 2.5 and 0.8 nm, respectively. The higher roughness, good catalytic activity, as well as the high conductivity further support the application of pyrite as a counter electrode. Moreover, the grain size from AFM was around 30–50 nm, which is consistent with the grain size obtained from SEM.

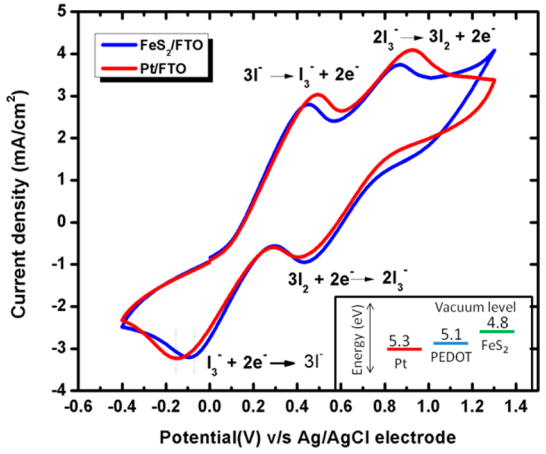

Figure 2. Cyclic voltammetry of FeS_2 and Pt electrodes with an iodine/tri-iodide redox electrolyte. Inset: work function of Pt, PEDOT, and FeS_2.

Several DSSCs were fabricated and tested with pyrite and Pt as counter electrodes with iodine/iodide-based electrolyte. Similarly, pyrite and PEDOT counter electrode cells were fabricated and tested with Co electrolyte. N719 dye was used for the I_3^-/I^- redox electrolyte cells, while C128 dye was used for the Co(III)/Co(II) redox electrolyte-mediated cells. Current density (*J*) *versus* photovoltage (*V*) characteristic plots obtained from these cells are shown in Figure 4. *J*–*V* curves plotted for Pt- and pyrite-based cells for different light intensities are also given in Supporting Information. Corresponding cell parameters are tabulated in Table 2.

Pyrite cells gave an efficiency of about 8.0%, which is higher than that of Pt (7.5%). Notably, the efficiency apparently increased as light intensity decreased from 1.0 to 0.5 Sun for both counter electrodes. However, at 0.1 Sun, both decreased, which could be due to the increase in dark current which leads to lower photovoltage (see Supporting Information Figure S3). For the cobalt electrolyte, the efficiency with the pyrite counter electrode (6.3%) was comparable to that of PEDOT (6.3%). The attributes of an "ideal" counter electrode are good catalytic activity and optimum work function for quick electron injection.[51] Our investigation clearly showed pyrite films to have good catalytic activity. The measured

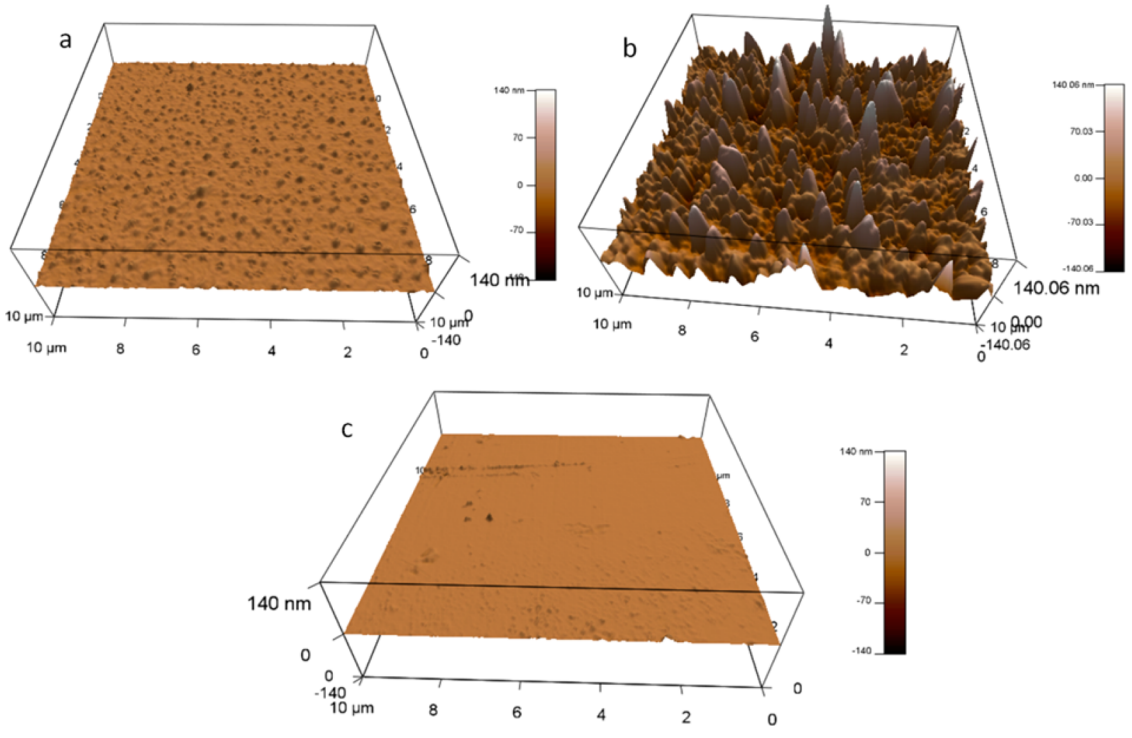

Figure 3. Surface morphology scan by AFM (tapping mode) of (a) Pt, (b) pyrite, and (c) PEDOT films.

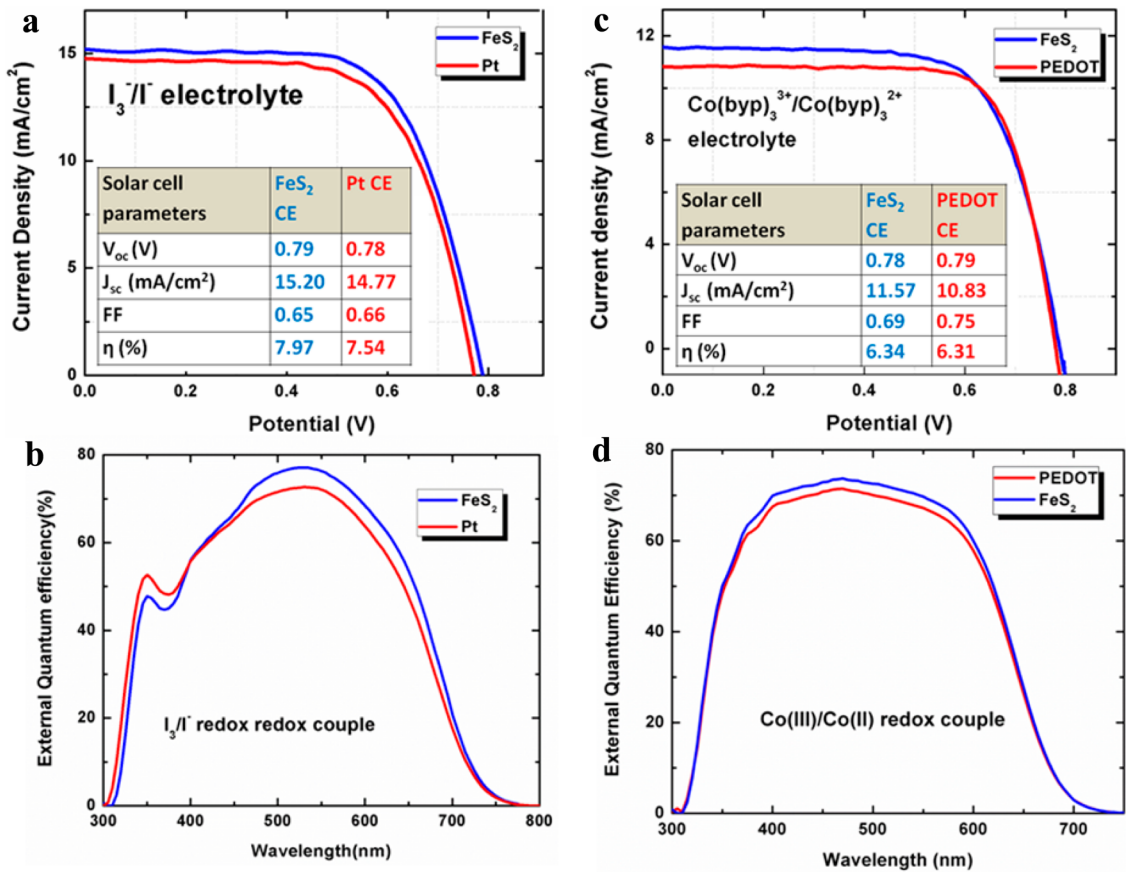

Figure 4. (a) $J-V$ curve and (b) IPCE of the FeS_2 and Pt counter electrode device with I_3^-/I^- electrolyte. (c) $J-V$ curve and (d) IPCE of the FeS_2 and PEDOT counter electrode with Co(III)/Co(II) electrolyte.

TABLE 2. FeS_2 and Pt Counter Electrode DSSC Parameters under Different Light Illumination Intensities

	1 Sun		0.5 Sun		0.1 Sun	
	FeS_2	Pt	FeS_2	Pt	FeS_2	Pt
V_{oc} (V)	0.79	0.78	0.75	0.74	0.68	0.66
J_{sc} (mA/cm^2)	15.20	14.77	8.97	8.91	1.75	1.74
FF	0.65	0.66	0.68	0.67	0.72	0.72
η (%)	7.97	7.54	9.27	8.92	8.68	8.32

work function found to be around 4.74 eV (by ultraviolet photoelectron spectroscopy), close to the values reported for pyrite single crystal and thin films[52−54] (Supporting Information Figure S4), was lower than the reported values of Pt (∼5.3 eV) and PEDOT (∼5.1 eV), which is advantageous for electron injection.[55,56]

Incident photon to electron conversion efficiency (IPCE) was found to be shifted upward in DSSCs with both iodine/iodide and cobalt electrolytes, as shown in Figure 4b,d when pyrite was used as the counter electrode in place of the conventional materials. Both spectra showed typical characteristics of the N719 dye and C128 dye. The upward shift of the IPCE curve is an indication that extra electrons are generated in the system. The shift is consistent with the increase in the value of J_{sc} apparent in the current density curves of

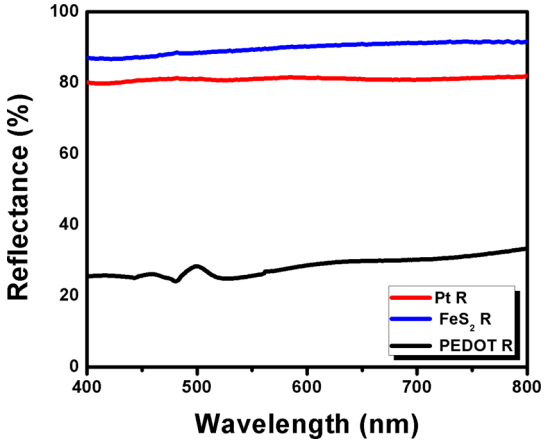

Figure 5. Reflectance FeS_2, PEDOT, and Pt thin films on FTO.

Figure 4a,b. For similar dye loading conditions, this increased photocurrent could be due to light reflection from the counter electrode. In order to verify this, the optical reflectance of the counter electrodes used was measured. The pyrite film exhibits higher reflectance than Pt (see Figure 5) and PEDOT. The reflected light will increase the photon absorption possibility in the active layer and consequently the light-harvesting efficiency. The increased photogeneration in the long wavelength region is consistent with the reflection of

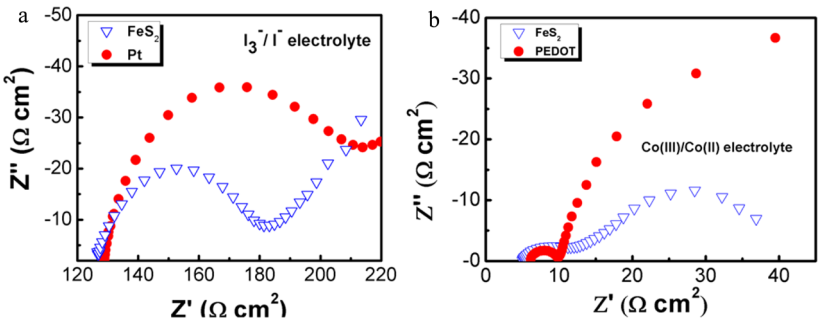

Figure 6. Electrochemical impedance spectra of (a) FeS_2 and Pt symmetric cells with I_3^-/I^- electrolyte and (b) FeS_2 and PEDOT symmetric cells with Co(III)/Co(II) electrolyte.

TABLE 3. Photovoltaic Cell Parameters from Pyrite CE and PEDOT CE Devices along with the Fitted Parameters Extracted from Impedance Spectroscopy of the Symmetric Cells

counter electrode	R_s[a] ($\Omega \cdot cm^2$)	R_{ct}[b] ($\Omega \cdot cm^2$)	C[c] (μF)	total R[d] ($\Omega \cdot cm^2$)
FeS_2	4.9	7.2	92	12.1
PEDOT	6.0	3.9	2.3	9.6

[a] Series resistance. [b] Charge transfer resistance. [c] Double-layer capacitance [d] $R = R_s + R_{ct}$.

light by the pyrite counter electrode. As expected, this light effect is less prominent at lower light intensities; therefore, the J_{sc} for Pt and pyrite devices is similar for lower light illuminations as in Table 2.

Symmetric cells were prepared in order to evaluate the electrochemical properties of the counter electrodes. Impedance spectroscopy is a widely used technique to characterize the charge transfer between semiconductors and electrolytes, which is a key parameter for a counter electrode.[57] In symmetric cells, two features are observable in the recorded spectra: a low-frequency feature that accounts for the electrolyte diffusion (not studied in this work) and a high-frequency arc due to the charge transfer in the interface.[58] The measurement of symmetric cells in the I_3^-/I^- electrolyte shows smaller high-frequency arc for FeS_2 than for Pt (see Figure 6a). A smaller high-frequency arc is caused by a lower charge transfer resistance from the electrolyte to the counter electrode. This confirms the higher catalytic activity of the FeS_2 counter electrode compared to the Pt one, which is also reflected in the overall performance of the solar cell device. This is not reflected in the final fill factor (FF) of the DSSC devices, probably due to the higher electrical conductivity of Pt which compensates for the lower catalytic effect and hence results in a similar total series resistance.[59]

The symmetric cell responses in the Co(III)/Co(II) electrolyte with FeS_2 and PEDOT electrodes were different. Parameters extracted from fitting the impedance data with the model are listed in Table 3. Total resistance R, which is the sum of the series resistance and charge transfer resistance, was calculated to be 12.1 $\Omega \cdot cm^2$, which is comparable to the value of 9.6 $\Omega \cdot cm^2$ of PEDOT. Impedance spectroscopy shows a higher charge transfer resistance for the FeS_2 sample (see Figure 6b), and consequently, a lower FF is observed for FeS_2 CEs. However, a double-layer capacitance value for pyrite was 92 μF, and for PEDOT, it was 2.3 μF. Higher double-layer capacitance values reflect an effectively high surface area of pyrite films resulting from its higher roughness of 34.9 nm compared to 0.8 mm for PEDOT demonstrated by AFM. This surface area increment of pyrite film compensates for the lower charge transfer resistance and results in overall comparable light conversion efficiency with PEDOT. This is confirmed by impedance measurement for the symmetric cell configuration.

CONCLUSION

We have demonstrated a pyrite (FeS_2) thin-film-based counter electrode in dye-sensitized solar cells. It has been found that pyrite films exhibited good catalytic activity compared to Pt in I_3^-/I^- and PEDOT in Co(III)/Co(II) electrolytes. Efficiencies are found to be superior to Pt counter electrodes and equivalent to PEDOT. The improvement in the overall performance of the pyrite CE-based cell is attributed to better catalytic activity of pyrite in conjunction with good optical reflectivity, which improves the light distribution in the solar cell to achieve maximum light efficiency. In summary, the results of this study provide a promising approach to reduce the cost and to enhance the performance of dye-sensitized solar cells by using earth abundant, more efficiently catalytic pyrite (FeS_2) films by a simple scalable spray pyrolysis technique.

METHODS

Preparation of FeS_2 Thin Films by Spray Pyrolysis. $FeCl_3 \cdot 6H_2O$ (Sigma-Aldrich) and NH_2CSNH_2 (Sigma-Aldrich) were used as precursors. A 50 mL solution of 0.1 M iron chloride and thiourea taken in a 1:6 ratio was prepared in DI water. As-prepared solution was sprayed by a spray gun with nitrogen carrier gas on the FTO substrate precleaned by ethanol and DI water. The deposited substrate was mounted on a hot plate at 330 °C to pyrolyze into FeS_2 thin film. Finally, the film was sulfurized at 400 °C for 30 min in argon atmosphere. Details are described in the Supporting Information.

FeS_2 Counter Electrode Device Fabrication. The N719 (Dyesol)-sensitized devices were fabricated as reported elsewhere.[60] Briefly, the FTO glass (2.2 mm thickness, 14 Ω/sq, Pilkington) used as current collector was first cleaned, then immersed into a 40 mM aqueous $TiCl_4$ solution at 70 °C for 30 min, and rinsed with water and ethanol. Next, 10 μm thick transparent TiO_2 layers (Dyesol 18NR-T, average nanoparticle size = 20 nm) were screen-printed on the FTO glass plates (mesh count is 90 T mesh/cm, active areas are 0.16 cm^2). After being dried at 125 °C, 5 μm thick scattering TiO_2 layers (Dyesol WER2-O paste, average nanoparticle size = 150−250 nm) were superimposed by screen-printing. The electrodes coated with the TiO_2 pastes were gradually annealed under air at 125 °C for 10 min, 325 °C for 5 min, 375 °C for 5 min, 450 °C for 15 min, and, finally, 500 °C for 15 min. The TiO_2 films which were again treated with 40 mM $TiCl_4$ solution for 30 min at 70 °C were rinsed with DI water and ethanol and annealed at 500 °C for 30 min. After being cooled to room temperature, the TiO_2photoanodes of optimum devices were made by immersing them into 0.3 mM N719 dye solution in a mixture of acetonitrile and *tert*-butyl alcohol (volume ratio 1:1) for 15 h. The dye-sensitized TiO_2 photoanode and the Pt-coated FTO glass counter electrode were sandwiched together using a 25 μm thick transparent Surlyn film (Meltonix 1170-25, Solaronix). The electrolyte was injected through the hole at the back of the counter electrode *via* vacuum backfilling. The electrolyte employed was a solution of containing 1.0 mM 1,3-dimethylimidazolium iodide, 50 mM LiI, 30 mM I_2, 0.5 mM *tert*-butylpyridine, and 0.1 mM guanidinium thiocyanate in the mixed solvent of acetonitrile and valeronitrile (v/v, 85/15).[61] Finally, the hole was sealed using 25 μm thick Surlyn and a cover glass (0.1 mm thickness) to avoid leakage of the electrolyte.

Fluorine-doped tin oxide (FTO) glass substrates (Pilkington, TEC15) were cleaned with Decon90 solution in an ultrasonic bath for 30 min, followed by washing with water and ethanol. Pre-$TiCl_4$ treatment was performed by dipping the cleaned glass substrates in a 40 mM aqueous $TiCl_4$ solution at 70 °C for 30 min. The substrates were then washed with water and ethanol. Mesoporous TiO_2 films (0.16 cm^2) were prepared by screen-printing colloidal TiO_2 paste and drying at 125 °C between deposition steps. Two layers of scattering TiO_2 layer (Dyesol WER2-O) were deposited on top of the mesoporous TiO_2 film. The electrodes with a total thickness of 9.5 μm were subsequently heated to 500 °C for 15 min with programmed temperature ramping. After sintering, the electrodes were treated again with 40 mM $TiCl_4$ at 70 °C for another 30 min and rinsed as above. A final heating process was performed at 500 °C for 30 min.

Once cooled, the electrodes were immersed in 0.2 mM of C218 in acetonitrile/*t*-butyl alcohol (2:1) for 15 h. Solar cells were assembled with a PEDOT counter electrode using a 25 μm thick hot-melt spacer (Surlyn, Dupont). Cobalt electrolyte containing 0.22 M $Co(bpy)_3(TFSI)_2$, 0.05 M $Co(bpy)_3(TFSI)_3$, 0.1 M LiTFSI, and 0.2 M TBP in acetonitrile was injected *via* two holes predrilled in the counter electrode and sealed with a Surlyn cover and a glass coverslip.

The PEDOT counter electrode was prepared by electropolymerization in a three-electrode configuration cell. The working electrode, a cleaned FTO substrate, was immersed into the cell containing 0.01 M of EDOT (Sigma-Aldrich) in 0.1 M aqueous sodium dodecyl sulfate (Sigma-Aldrich) solution. Stainless steel grid and a leak-free Ag/AgCl electrode were used as counter and reference electrodes, respectively. The PEDOT film was deposited potentiostatically using a dc potential of 1.2 V for 30 s. The PEDOT counter electrode was subsequently rinsed with deionized water and ethanol.

Characterization. Thin film X-ray diffraction data were taken by a Bruker D8 Advance diffractometer using Cu Kα radiation. T64000 micro-Raman spectrometer with an incident laser power of 0.18 mW and excitation wavelength of 532 nm was used for Raman phase analysis. SEM images were acquired from a field-emission scanning electron microscope (JEOL JSM-7600F). Substrates were sputtered with 10 nm Pt prior to the SEM imaging. UV−vis optical reflection and transmission measurements were performed using a PerkinElmer Lambda 950 spectrophotometer with an integrating sphere. Hall and Van der Pauw measurements were performed by a NMR variable-temperature Hall measurement system using four probes.

Cyclic voltammetry and impedance spectroscopy were performed using an Autolab potentiostat (PGSTAT 302). A voltage perturbation of 20 mV was applied from 400 kHz to 1 Hz for impedance spectrum collection. Scan rate for CV was 100 mV s^{-1}.

Photovoltaic Measurements. Photocurrent density−photovoltage (*J*−*V*) characteristics were measured under an illumination of AM 1.5 (100 mW cm^{-2}) using a solar simulator (San-EI Electric, XEC-301S) equipped with a 450 W xenon lamp, which was coupled with an Agilent semiconductor parameter analyzer (4155C). The power of the simulated light was calibrated to 100 mW/cm^2 by using a silicon reference cell (Fraunhofer) and monitored using a power meter throughout the testing. A black mask (6 mm × 6 mm) was used in the subsequent photovoltaic studies to avoid the effects of diffusive light on cell performance.

Conflict of Interest: The authors declare no competing financial interest.

Acknowledgment. Q.X. would like to thank the Singapore National Research Foundation *via* a fellowship grant (NRF-RF2009-06), start-up grant (M58110061), and New Initiative Fund (M58110100) from Nanyang Technological University. The authors would like to gratefully acknowledge the Singapore−Berkeley Research Initiative for Sustainable Energy (SinBeRISE) CREATE programme. The authors would also like to thank Rohit Abraham, Prof. Lydia Helena Wong, and Prof. Subodh Mhaisalkar for fruitful discussions.

Supporting Information Available: Additional experimental details, figures, and table. This material is available free of charge *via* the Internet at http://pubs.acs.org.

REFERENCES AND NOTES

1. Ennaoui, A.; Tributsch, H. Iron Sulphide Solar Cells. *Sol. Cells* **1984**, *13*, 197–200.
2. Berry, N.; Cheng, M.; Perkins, C. L.; Limpinsel, M.; Hemminger, J. C.; Law, M. Atmospheric-Pressure Chemical Vapor Deposition of Iron Pyrite Thin Films. *Adv. Energy Mater.* **2012**, *2*, 1124–1135.
3. Limpinsel, M.; Farhi, N.; Berry, N.; Lindemuth, J.; Perkins, C. L.; Lin, Q.; Law, M. An Inversion Layer at the Surface of n-Type Iron Pyrite. *Energy Environ. Sci.* **2014**, *7*, 1974–1989.
4. Ge, H.; Hai, L.; Prabhakar, R. R.; Ming, L. Y.; Sritharan, T. Evolution of Nanoplate Morphology, Structure and Chemistry during Synthesis of Pyrite by a Hot Injection Method. *RSC Adv.* **2014**, *4*, 16489–16496.
5. Ennaoui, A.; Fiechter, S.; Pettenkofer, C.; Alonso-Vante, N.; Büker, K.; Bronold, M.; Höpfner, C.; Tributsch, H. Iron Disulfide for Solar Energy Conversion. *Sol. Energy Mater. Sol. Cells* **1993**, *29*, 289–370.
6. Susac, D.; Zhu, L.; Teo, M.; Sode, A.; Wong, K. C.; Wong, P. C.; Parsons, R. R.; Bizzotto, D.; Mitchell, K. A. R.; Campbell, S. A. Characterization of FeS_2-Based Thin Films as Model Catalysts for the Oxygen Reduction Reaction. *J. Phys. Chem. C* **2007**, *111*, 18715–18723.
7. Liu, G.; Li, X.; Wang, H.; Rong, Y.; Ku, Z.; Xu, M.; Liu, L.; Hu, M.; Yang, Y.; Han, H. A Class of Carbon Supported Transition Metal−Nitrogen Complex Catalysts for Dye-Sensitized Solar Cells. *J. Mater. Chem. A* **2013**, *1*, 1475–1480.
8. Seefeld, S.; Limpinsel, M.; Liu, Y.; Farhi, N.; Weber, A.; Zhang, Y.; Berry, N.; Kwon, Y. J.; Perkins, C. L.; Hemminger, J. C.; Wu, R.; Law, M. Iron Pyrite Thin Films Synthesized from an $Fe(acac)_3$ Ink. *J. Am. Chem. Soc.* **2013**, *135*, 4412–4424.
9. O'Regan, B.; Grätzel, M. A Low-Cost, High-Efficiency Solar Cell Based on Dye-Sensitized Colloidal TiO_2 Films. *Nature* **1991**, *353*, 737–740.
10. Kalowekamo, J.; Baker, E. Estimating the Manufacturing Cost of Purely Organic Solar Cells. *Sol. Energy* **2009**, *83*, 1224–1231.
11. Unold, T.; Schock, H. W. Nonconventional (Non-Silicon-Based) Photovoltaic Materials. *Annu. Rev. Mater. Res.* **2011**, *41*, 297–321.

12. Grätzel, M. Photoelectrochemical Cells. *Nature* **2001**, *414*, 338–344.
13. Ardo, S.; Meyer, G. J. Photodriven Heterogeneous Charge Transfer with Transition-Metal Compounds Anchored to TiO_2 Semiconductor Surfaces. *Chem. Soc. Rev.* **2009**, *38*, 115–164.
14. Fan, Z.; Ruebusch, D.; Rathore, A.; Kapadia, R.; Ergen, O.; Leu, P.; Javey, A. Challenges and Prospects of Nanopillar-Based Solar Cells. *Nano Res.* **2009**, *2*, 829–843.
15. Hagfeldt, A.; Boschloo, G.; Sun, L.; Kloo, L.; Pettersson, H. Dye-Sensitized Solar Cells. *Chem. Rev.* **2010**, *110*, 6595–6663.
16. Tian, H.; Yu, Z.; Hagfeldt, A.; Kloo, L.; Sun, L. Organic Redox Couples and Organic Counter Electrode for Efficient Organic Dye-Sensitized Solar Cells. *J. Am. Chem. Soc.* **2011**, *133*, 9413–9422.
17. Yella, A.; Lee, H.-W.; Tsao, H. N.; Yi, C.; Chandiran, A. K.; Nazeeruddin, M. K.; Diau, E. W.-G.; Yeh, C.-Y.; Zakeeruddin, S. M.; Grätzel, M. Porphyrin-Sensitized Solar Cells with Cobalt (II/III)-Based Redox Electrolyte Exceed 12% Efficiency. *Science* **2011**, *334*, 629–634.
18. Mathew, S.; Yella, A.; Gao, P.; Humphry-Baker, R.; Curchod, B. F. E.; Ashari-Astani, N.; Tavernelli, I.; Rothlisberger, U.; Nazeeruddin, M. K.; Grätzel, M. Dye-Sensitized Solar Cells with 13% Efficiency Achieved through the Molecular Engineering of Porphyrin Sensitizers. *Nat. Chem.* **2014**, *6*, 242–247.
19. Bao, C.; Huang, H.; Yang, J.; Gao, H.; Yu, T.; Liu, J.; Zhou, Y.; Li, Z.; Zou, Z. The Maximum Limiting Performance Improved Counter Electrode Based on a Porous Fluorine Doped Tin Oxide Conductive Framework for Dye-Sensitized Solar Cells. *Nanoscale* **2013**, *5*, 4951–4957.
20. Ghamouss, F.; Pitson, R.; Odobel, F.; Boujtita, M.; Caramori, S.; Bignozzi, C. A. Characterization of Screen Printed Carbon Counter Electrodes for Co(II)/(III) Mediated Photoelectrochemical Cells. *Electrochim. Acta* **2010**, *55*, 6517–6522.
21. Yun, S.; Wu, M.; Wang, Y.; Shi, J.; Lin, X.; Hagfeldt, A.; Ma, T. Pt-like Behavior of High-Performance Counter Electrodes Prepared from Binary Tantalum Compounds Showing High Electrocatalytic Activity for Dye-Sensitized Solar Cells. *ChemSusChem* **2013**, *6*, 411–416.
22. Jeong, I.; Jo, C.; Anthonysamy, A.; Kim, J.-M.; Kang, E.; Hwang, J.; Ramasamy, E.; Rhee, S.-W.; Kim, J. K.; Ha, K.-S.; Jun, K.-W.; Lee, J. Ordered Mesoporous Tungsten Suboxide Counter Electrode for Highly Efficient Iodine-Free Electrolyte-Based Dye-Sensitized Solar Cells. *ChemSusChem* **2013**, *6*, 299–307.
23. Mulmudi, H. K.; Batabyal, S. K.; Rao, M.; Prabhakar, R. R.; Mathews, N.; Lam, Y. M.; Mhaisalkar, S. G. Solution Processed Transition Metal Sulfides: Application as Counter Electrodes in Dye Sensitized Solar Cells (DSCs). *Phys. Chem. Chem. Phys.* **2011**, *13*, 19307–19309.
24. Wu, M.; Zhang, Q.; Xiao, J.; Ma, C.; Lin, X.; Miao, C.; He, Y.; Gao, Y.; Hagfeldt, A.; Ma, T. Two Flexible Counter Electrodes Based on Molybdenum and Tungsten Nitrides for Dye-Sensitized Solar Cells. *J. Mater. Chem.* **2011**, *21*, 10761–10766.
25. Li, G. R.; Song, J.; Pan, G. L.; Gao, X. P. Highly Pt-like Electrocatalytic Activity of Transition Metal Nitrides for Dye-Sensitized Solar Cells. *Energy Environ. Sci.* **2011**, *4*, 1680–1683.
26. Guo, W.; Shen, Y.; Wu, M.; Wang, L.; Wang, L.; Ma, T. SnS-Quantum Dot Solar Cells Using Novel TiC Counter Electrode and Organic Redox Couples. *Chem.—Eur. J.* **2012**, *18*, 7862–7868.
27. Fang, B.; Fan, S.-Q.; Kim, J. H.; Kim, M.-S.; Kim, M.; Chaudhari, N. K.; Ko, J.; Yu, J.-S. Incorporating Hierarchical Nanostructured Carbon Counter Electrode into Metal-Free Organic Dye-Sensitized Solar Cell. *Langmuir* **2010**, *26*, 11238–11243.
28. Zhang, L.; Mulmudi, H. K.; Batabyal, S. K.; Lam, Y. M.; Mhaisalkar, S. G. Metal/Metal Sulfide Functionalized Single-Walled Carbon Nanotubes: FTO-Free Counter Electrodes for Dye Sensitized Solar Cells. *Phys. Chem. Chem. Phys.* **2012**, *14*, 9906–9911.
29. Roy-Mayhew, J. D.; Bozym, D. J.; Punckt, C.; Aksay, I. A. Functionalized Graphene as a Catalytic Counter Electrode in Dye-Sensitized Solar Cells. *ACS Nano* **2010**, *4*, 6203–6211.
30. Yang, Z.; Liu, M.; Zhang, C.; Tjiu, W. W.; Liu, T.; Peng, H. Carbon Nanotubes Bridged with Graphene Nanoribbons and Their Use in High-Efficiency Dye-Sensitized Solar Cells. *Angew. Chem., Int. Ed.* **2013**, *52*, 3996–3999.
31. Khaderbad, M. A.; Tjoa, V.; Oo, T. Z.; Wei, J.; Sheri, M.; Mangalampalli, R.; Rao, V. R.; Mhaisalkar, S. G.; Mathews, N. Facile Fabrication of Graphene Devices through Metalloporphyrin Induced Photocatalytic Reduction. *RSC Adv.* **2012**, *2*, 4120–4124.
32. Hong, W.; Xu, Y.; Lu, G.; Li, C.; Shi, G. Transparent Graphene/PEDOT—PSS Composite Films as Counter Electrodes of Dye-Sensitized Solar Cells. *Electrochem. Commun.* **2008**, *10*, 1555–1558.
33. Kavan, L.; Yum, J.-H.; Nazeeruddin, M. K.; Grätzel, M. Graphene Nanoplatelet Cathode for Co(III)/(II) Mediated Dye-Sensitized Solar Cells. *ACS Nano* **2011**, *5*, 9171–9178.
34. Yoo, D.; Kim, J.; Kim, J. Direct Synthesis of Highly Conductive Poly(3,4-ethylenedioxythiophene):Poly(4-styrenesulfonate) (PEDOT:PSS)/Graphene Composites and Their Applications in Energy Harvesting Systems. *Nano Res.* **2014**, *7*, 717–730.
35. Wang, Y.-C.; Wang, D.-Y.; Jiang, Y.-T.; Chen, H.-A.; Chen, C.-C.; Ho, K.-C.; Chou, H.-L.; Chen, C.-W. FeS_2 Nanocrystal Ink as a Catalytic Electrode for Dye-Sensitized Solar Cells. *Angew. Chem., Int. Ed.* **2013**, *52*, 6694–6698.
36. Dong, A.; Ye, X.; Chen, J.; Kang, Y.; Gordon, T.; Kikkawa, J. M.; Murray, C. B. A Generalized Ligand-Exchange Strategy Enabling Sequential Surface Functionalization of Colloidal Nanocrystals. *J. Am. Chem. Soc.* **2011**, *133*, 998–1006.
37. Prabhakar, R. R.; Pramana, S. S.; Karthik, K. R. G.; Sow, C. H.; Jinesh, K. B. Ultra-thin Conformal Deposition of $CuInS_2$ on ZnO Nanowires by Chemical Spray Pyrolysis. *J. Mater. Chem.* **2012**, *22*, 13965–13968.
38. Kaelin, M.; Rudmann, D.; Tiwari, A. N. Low Cost Processing of CIGS Thin Film Solar Cells. *Sol. Energy* **2004**, *77*, 749–756.
39. Kloc, C.; Willeke, G.; Bucher, E. Flux Growth and Electrical Transport Measurements of Pyrite (FeS_2). *J. Cryst. Growth* **1993**, *131*, 448–452.
40. Verble, J. L.; Wallis, R. F. Infrared Studies of Lattice Vibrations in Iron Pyrite. *Phys. Rev.* **1969**, *182*, 783–789.
41. Ushioda, S. Raman Scattering from Phonons in Iron Pyrite (FeS_2). *Solid State Commun.* **1972**, *10*, 307–310.
42. Bonnissel-Gissinger, P.; Alnot, M.; Ehrhardt, J.-J.; Behra, P. Surface Oxidation of Pyrite as a Function of pH. *Environ. Sci. Technol.* **1998**, *32*, 2839–2845.
43. Nesbitt, H. W.; Muir, I. J. X-ray Photoelectron Spectroscopic Study of a Pristine Pyrite Surface Reacted with Water Vapour and Air. *Geochim. Cosmochim. Acta* **1994**, *58*, 4667–4679.
44. Grosvenor, A. P.; Kobe, B. A.; Biesinger, M. C.; McIntyre, N. S. Investigation of Multiplet Splitting of Fe 2p XPS Spectra and Bonding in Iron Compounds. *Surf. Interface Anal.* **2004**, *36*, 1564–1574.
45. Mycroft, J. R.; Bancroft, G. M.; McIntyre, N. S.; Lorimer, J. W.; Hill, I. R. Detection of Sulphur and Polysulphides on Electrochemically Oxidized Pyrite Surfaces by X-ray Photoelectron Spectroscopy and Raman Spectroscopy. *J. Electroanal Chem. Interfacial Electrochem.* **1990**, *292*, 139–152.
46. Nesbitt, H. W.; Bancroft, G. M.; Pratt, A. R.; Scaini, M. J. Sulfur and Iron Surface States on Fractured Pyrite Surfaces. *Am. Mineral.* **1998**, *83*, 1067–1076.
47. Eggleston, C. M.; Ehrhardt, J.-J.; Stumm, W. Surface Structural Controls on Pyrite Oxidation Kinetics: An XPS-UPS, STM, and Modeling Study. *Am. Mineral.* **1996**, *81*, 1036–1056.
48. Mooney, J. B.; Radding, S. B. Spray Pyrolysis Processing. *Annu. Rev. Mater. Sci.* **1982**, *12*, 81–101.
49. Zhang, X.; Manno, M.; Baruth, A.; Johnson, M.; Aydil, E. S.; Leighton, C. Crossover from Nanoscopic Intergranular Hopping to Conventional Charge Transport in Pyrite Thin Films. *ACS Nano* **2013**, *7*, 2781–2789.
50. Daeneke, T.; Kwon, T.-H.; Holmes, A. B.; Duffy, N. W.; Bach, U.; Spiccia, L. High-Efficiency Dye-Sensitized Solar Cells

with Ferrocene-Based Electrolytes. *Nat. Chem.* **2011**, *3*, 211–215.
51. Hou, Y.; Wang, D.; Yang, X. H.; Fang, W. Q.; Zhang, B.; Wang, H. F.; Lu, G. Z.; Hu, P.; Zhao, H. J.; Yang, H. G. Rational Screening Low-Cost Counter Electrodes for Dye-Sensitized Solar Cells. *Nat. Commun.* **2013**, *4*, 1583.
52. Pettenkofer, C.; Jaegermann, W.; Bronold, M. Site Specific Surface Interaction of Electron Donors and Acceptors on FeS_2(100) Cleavage Planes. *Ber. Bunsen-Ges.* **1991**, *95*, 560–565.
53. Wang, D.-Y.; Jiang, Y.-T.; Lin, C.-C.; Li, S.-S.; Wang, Y.-T.; Chen, C.-C.; Chen, C.-W. Solution-Processable Pyrite FeS_2 Nanocrystals for the Fabrication of Heterojunction Photodiodes with Visible to NIR Photodetection. *Adv. Mater.* **2012**, *24*, 3415–3420.
54. Ennaoui, A.; Fiechter, S.; Tributsch, H.; Giersig, M.; Vogel, R.; Weller, H. Photoelectrochemical Energy Conversion Obtained with Ultrathin Organo-Metallic-Chemical-Vapor-Deposition Layer of FeS_2 (Pyrite) on TiO_2. *J. Electrochem. Soc.* **1992**, *139*, 2514–2518.
55. Guerrero, A.; Marchesi, L. F.; Boix, P. P.; Ruiz-Raga, S.; Ripolles-Sanchis, T.; Garcia-Belmonte, G.; Bisquert, J. How the Charge-Neutrality Level of Interface States Controls Energy Level Alignment in Cathode Contacts of Organic Bulk-Heterojunction Solar Cells. *ACS Nano* **2012**, *6*, 3453–3460.
56. Li, S.-S.; Tu, K.-H.; Lin, C.-C.; Chen, C.-W.; Chhowalla, M. Solution-Processable Graphene Oxide as an Efficient Hole Transport Layer in Polymer Solar Cells. *ACS Nano* **2010**, *4*, 3169–3174.
57. Fabregat-Santiago, F.; Garcia-Belmonte, G.; Mora-Sero, I.; Bisquert, J. Characterization of Nanostructured Hybrid and Organic Solar Cells by Impedance Spectroscopy. *Phys. Chem. Chem. Phys.* **2011**, *13*, 9083–9118.
58. Boix, P. P.; Lee, Y. H.; Fabregat-Santiago, F.; Im, S. H.; Mora-Sero, I.; Bisquert, J.; Seok, S. I. From Flat to Nanostructured Photovoltaics: Balance between Thickness of the Absorber and Charge Screening in Sensitized Solar Cells. *ACS Nano* **2012**, *6*, 873–880.
59. Trevisan, R.; Döbbelin, M.; Boix, P. P.; Barea, E. M.; Tena-Zaera, R.; Mora-Seró, I.; Bisquert, J. PEDOT Nanotube Arrays as High Performing Counter Electrodes for Dye Sensitized Solar Cells. Study of the Interactions Among Electrolytes and Counter Electrodes. *Adv. Energy Mater.* **2011**, *1*, 781–784.
60. Ito, S.; Murakami, T. N.; Comte, P.; Liska, P.; Grätzel, C.; Nazeeruddin, M. K.; Grätzel, M. Fabrication of Thin Film Dye Sensitized Solar Cells with Solar to Electric Power Conversion Efficiency Over 10%. *Thin Solid Films* **2008**, *516*, 4613–4619.
61. Chen, C.-Y.; Wang, M.; Li, J.-Y.; Pootrakulchote, N.; Alibabaei, L.; Ngoc-le, C.-h.; Decoppet, J.-D.; Tsai, J.-H.; Grätzel, C.; Wu, C.-G.; Zakeeruddin, S. M.; Grätzel, M. Highly Efficient Light-Harvesting Ruthenium Sensitizer for Thin-Film Dye-Sensitized Solar Cells. *ACS Nano* **2009**, *3*, 3103–3109.